Preprint
UCRL-JC-145561

Aseismic Slip Events along the Southern San Andreas Fault System Captured by Radar Interferometry

P. Vincent

This article was submitted to the 3rd Conference on Tectonic Problems of the San Andreas Fault System, Stanford, California, September 6-8, 2000

U.S. Department of Energy

Lawrence
Livermore
National
Laboratory

October 1, 2001

DISCLAIMER

This document was prepared as an account of work sponsored by an agency of the United States Government. Neither the United States Government nor the University of California nor any of their employees, makes any warranty, express or implied, or assumes any legal liability or responsibility for the accuracy, completeness, or usefulness of any information, apparatus, product, or process disclosed, or represents that its use would not infringe privately owned rights. Reference herein to any specific commercial product, process, or service by trade name, trademark, manufacturer, or otherwise, does not necessarily constitute or imply its endorsement, recommendation, or favoring by the United States Government or the University of California. The views and opinions of authors expressed herein do not necessarily state or reflect those of the United States Government or the University of California, and shall not be used for advertising or product endorsement purposes.

This is a preprint of a paper intended for publication in a journal or proceedings. Since changes may be made before publication, this preprint is made available with the understanding that it will not be cited or reproduced without the permission of the author.

This report has been reproduced directly from the best available copy.

Available electronically at http://www.doc.gov/bridge

Available for a processing fee to U.S. Department of Energy
And its contractors in paper from
U.S. Department of Energy
Office of Scientific and Technical Information
P.O. Box 62
Oak Ridge, TN 37831-0062
Telephone: (865) 576-8401
Facsimile: (865) 576-5728
E-mail: reports@adonis.osti.gov

Available for the sale to the public from
U.S. Department of Commerce
National Technical Information Service
5285 Port Royal Road
Springfield, VA 22161
Telephone: (800) 553-6847
Facsimile: (703) 605-6900
E-mail: orders@ntis.fedworld.gov
Online ordering: http://www.ntis.gov/ordering.htm

OR

Lawrence Livermore National Laboratory
Technical Information Department's Digital Library
http://www.llnl.gov/tid/Library.html

ASEISMIC SLIP EVENTS ALONG THE SOUTHERN SAN ANDREAS FAULT SYSTEM CAPTURED BY RADAR INTERFEROMETRY

Paul Vincent
Lawrence Livermore National Laboratory, Livermore, CA 94550

ABSTRACT

Aseismic slip is observed along several faults in the Salton Sea and southernmost Landers rupture zone regions using interferometric synthetic aperture radar (InSAR) data spanning different time periods between 1992 and 1997. In the southernmost Landers rupture zone, projecting south from the Pinto Mountain Fault, sharp discontinuities in the interferometric phase are observed along the sub-parallel Burnt Mountain and Eureka Peak Faults beginning three months after the Landers earthquake and is interpreted to be post-Landers after-slip. Abrupt phase offsets are also seen along the two southernmost contiguous 11 km Durmid Hill and North Shore segments of the San Andreas Fault with an abrupt termination of slip near the northern end of the North Shore Segment. A sharp phase offset is seen across 20 km of the 30 km-long Superstition Hills Fault before phase decorrelation in the Imperial Valley along the southern 10 km of the fault prevents coherent imaging by InSAR. A time series of deformation interferogrms suggest most of this slip occurred between 1993 and 1995 and none of it occurred between 1992 and 1993. A phase offset is also seen along a 5 km central segment of the Coyote Creek fault that forms a wedge with an adjoining northeast-southwest trending conjugate fault. Most of the slip observed on the southern San Andreas and Superstition Hills Faults occurred between 1993 and 1995--no slip is observed in the 92-93 interferograms. These slip events, especially the Burnt Mountain and Eureka Peak events, are inferred to be related to stress redistribution from the June, 1992 M_w= 7.3 Landers earthquake. Best-fit elastic models of the San Andreas and Superstition Hills slip events suggest source mechanisms with seismic moments over three orders of magnitude larger than a maximum possible summation of seismic moments from all seismicity along each fault segment during the entire 4.8-year time interval spanned by the InSAR data. Aseismic moment releases of this magnitude (equivalent to Mw = 5.3 and 5.6 events on the Superstition Hills and San Andreas Faults respectively) are hitherto unknown and have not been captured previously by any geodetic technique.

INTRODUCTION

SAR interferometry is rapidly becoming a new geodetic standard for detecting and measuring subtle changes in the Earth’s land and ice surfaces over periods of days to years with sub-centimeter accuracy and global, day or night, all weather accessibility. While the majority of earlier InSAR-based deformation studies focused on relatively large deformation gradients (>5 cm/ km) occurring over short time periods (days to months) [e.g., Goldstein et al., 1993; Massonnet, et al., 1993; Peltzer and Rosen, 1995;] recently InSAR studies have begun to focus on smaller deformation gradients occurring over longer time periods (one to several years) [e.g., Rosen, et al.,1998; Vincent, 1998, Burgmann, et al, 1998]. These smaller interseismic deformations are often more revealing when characterizing potential earthquake hazards.

In this study we examine aseismic slip along the southernmost San Andreas fault system from just north of the U.S./Mexico border to the Pinto Mountain fault during the period 8/4/92 to 1/24/97 (4.8 years) using SAR interferometry (see Figure 1). The InSAR data capture both 1) aseismic post-Landers after-slip events on the Eureka Peak and Burnt

Mountain faults in the southern Landers rupture zone and 2) aseismic, potentially triggered slip on faults in the Salton Sea region over 100 kilometers away to the south. While there is good agreement between the InSAR results and conventional geodetic measurements where available (for example, after-slip on the Eureka Peak and Burnt Mountain faults following the Landers Earthquake [Behr, et al., 1994]) the slip events on the southern SAF and Superstition Hills faults were not captured by other geodetic measurements. In addition, the InSAR results provide a spatially quasi-continuous map of the deformation field showing how the deformation varies both across and along strike of the imaged faults. Unlike creepmeter measurements that sample only the near field, or sparsely-distributed GPS measurements that typically sample only the far-field, InSAR samples both the near and far field providing better surface spatial constraints and an additional depth constraint allowing for more accurate fault slip models and geodetic moment calculations.

Numerical (elastic) models constrained by near-field (creepmeters, leveling, alignment arrays, etc.) and far-field (GPS, trilateration) data, were compared with the interferograms to find the best-fit slip event source parameters. The relatively complex deformation field associated with the interacting, sub-parallel, closely spaced Eureka Peak and Burnt Mountain fault slip events captured in the interferogram are predicted to a surprising degree of accuracy by the best-fit model simply by imposing the geodetically-constrained right-lateral after-slip on both faults. In the case of the triggered slip on the southern San Andreas and Superstition Hills faults, the best-fit models require a seismic moment release for each event that is several orders of magnitude greater than the total seismic moment obtained from summing all recorded seismicity for each fault segment during the same time interval. This result has important implications for our current understanding of the nature of seismic energy release associated with fault slip.

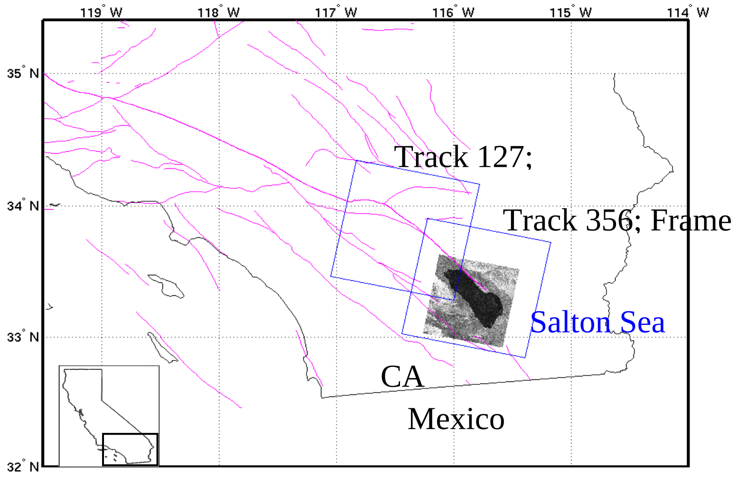

Figure 1:. Location and overlay map of ERS SAR data frames used in this study shown with the mapped surface traces of the major faults in the region.

TECTONIC SETTING

Pinto Mountain/South Landers Rupture Zone

The San Andreas fault system in the northern Coachella Valley northwest of the Salton Sea, is dominated by the left-lateral conjugate Pinto Mountain fault system. This fault system, which includes the Eureka Peak, Burnt Mountain, Homestead Valley, and Morongo Valley faults, as well as the Landers rupture zone faults (Homestead Valley, Johnson Valley, Kickapoo, Emerson, Camp Rock, and Landers faults), are all part of a fault system that transfers stress from the San Andreas to the Eastern California Shear Zone. On June 29th, 1992 the Mw=7.3 Landers earthquake ruptured an 85 km segment of this shear zone from 10 km south of Yucca Valley to approximately 15 km southeast of Barstow, California [Sieh, et al., 1993]. The earthquake produced an average of 3 meters and a high of 6.2 meters of right-lateral displacement along the rupture zone [Sieh, et al, 1992; Hart et al., 1992; Sieh, et al., 1993]. Post-seismic displacements following the earthquake have been measured by GPS networks, trilateration arrays and creepmeters from days to years after the earthquake. GPS measurements indicated that less than 10 cm of post-seismic displacement occurred along the north and central part of the rupture zone and up to 18 cm of post-seismic displacement occurred along the southern Johnson Valley and Eureka Peak faults during the first year following the earthquake [Shen, et al., 1994]. Creepmeters were installed at several locations along the Johnson Valley, Eureka Peak, and Burnt Mountain faults to measure continued slip but only the Eureka Peak fault showed significant after-slip of 8 cm in the 4 days following the earthquake [Behr, et al., 1994].

The Eureka Peak and Burnt Mountain faults are approximately 20 km each, roughly north-south oriented, right-lateral strike-slip faults. It is thought that the April 22, 1992 Mw=6.1 Joshua Tree earthquake rupture (a precursor to the June 29th, 1992 Landers earthquake) occurred on the Eureka Peak fault. The faults were actually unknown until the subsequent Landers earthquake where rupture on the southernmost 10 kilometers of the Eureka Peak fault (21 centimeter surface offset) made its presence known [Jennings, 1994]. The 1992 Landers rupture on the Eureka fault occurred in two separate, but close in time, events. The first ground breakage occurred some 30 seconds after the main shock was felt in the Yucca Valley. The second rupture episode was thought to be linked to a magnitude 5.6 aftershock less than 3 minutes after the Landers mainshock [Jennings, 1994]. Additional movement on the fault is postulated to have occurred as after-slip. The long-term (geologically-determined) slip rates on these two faults are estimated at about 0.5-0.6 mm/yr [Jennings, 1994].

Salton Sea

The Salton Sea in Southern California is located at the southernmost end of the San Andreas fault and is a region dominated by extensional subsidence due to a right step-over between the southern end of the San Adreas fault and the beginning of the Imperial fault (See Figure 2). Between the southernmost end of the San Andreas fault and the northernmost end of the Imperial fault is the Brawley Seismic Zone (BSZ), the northernmost extent (and youngest) of a series of small spreading centers offset by transform faults that extend southward into the Gulf of California and eventually become the East Pacific Rise. Located along the southernmost end of the San Andreas fault is Durmid Hill, an elongate hill approximately 20 km long and 4 km wide, rising about 100 m above the Salton Sea. Leveling data show that Durmid Hill is rising 1 to 2 millimeters per year and studies suggest this is caused by a component of fault normal convergence at Durmid Hill [Sylvester, et al., 1993]. The southern end of the San Andreas fault at Durmid Hill is one of the least seismically active regions in southern California [see Figure 2 from Larsen and Reilinger, 1992] and is interpreted to be due to a locked fault segment that releases its strain infrequently in large to great earthquakes [Sieh and Williams, 1990].

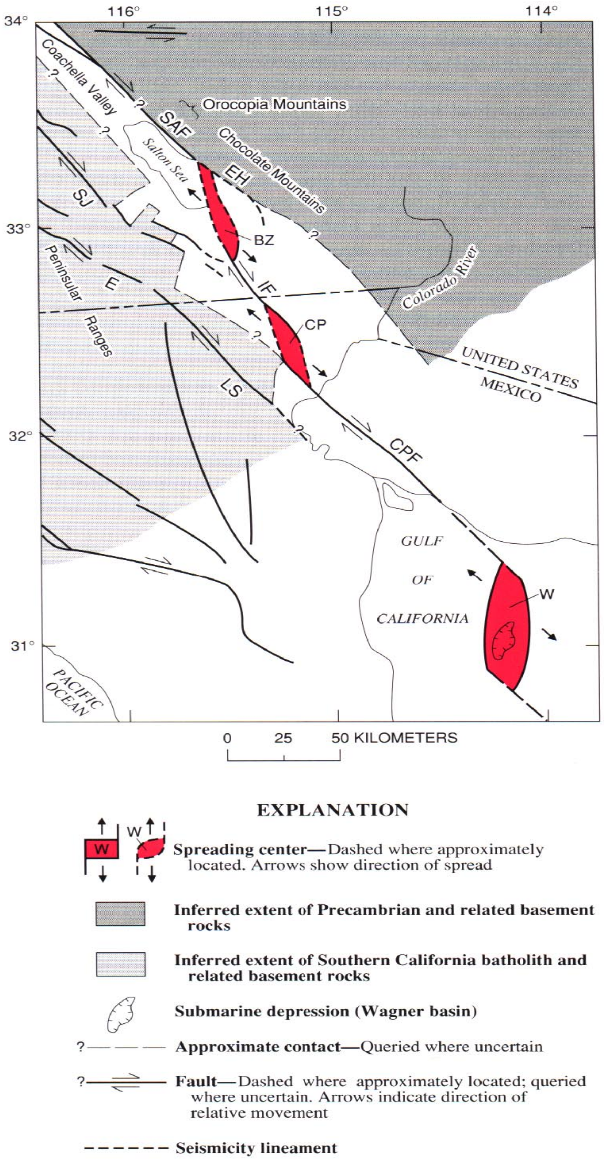

Figure 2: Salton Trough and Gulf of California showing spreading centers and southern termination of the San Andreas fault [from Wallace, 1990].

INSAR DATA AND PROCESSING

Data from three different ERS satellite track/frame combinations were used in this study. Track 127, frame 2925 (scene center: lat.: 33.83_; lon: -116.54_) is centered over the northern Coachella Valley and captures the post-Landers after-slip on the Burnt Mountain and Eureka Peak faults as well as the triggered slip on the San Andreas fault to the south. Track 356, frames 2925 (shifted south 50 km) and 2933 (scene center: lat. = 33.42_, lon. = -115.8) is centered over the Salton Sea and captures the same triggered slip on the San Andreas fault as track/frame 127/2925 to the north, as well as triggered slip on the Superstition Hills and Coyote Creek faults. The frames each cover an approximate 100 km by 100 km area and are shown along with the mapped surface traces of the major faults of the region in Figure 1. The data were processed using JPL IntSoft software to form both the single-look complex images (SLCs) and the interferograms. Table 1 shows the orbit pairs used, the time interval between orbits, the perpendicular component of the repeat-orbit baseline, and the ambiguity height for each orbit pair. The smaller the perpendicular component of the baseline is (i.e., the distance between satellite imaging positions between the reference and slave orbit passes), the less sensitive the interferometric phase is to topography. The sensitivity of the phase to topography is also reflected in the ambiguity height value, which is inversely proportional to the perpendicular baseline. The ambiguity height represents the amount of topographic change necessary to produce one interferometric fringe. The larger this number is the less ambiguous the phase signal is between representing deformation verses representing (imperfectly removed) topography.

Table 1. ERS orbit pairs used with relevant interferometric parameters.

Reference Sat./Orbit.Frame	Date	Slave Sat./Orbit/Frame	Date	ΔT days/years	Perp. Baseline	Ambig. Height
E1/5511.2925	920804	E1/8517.2933	930302	328 / 0.8986	16m	570m
E1/5511.2925	920804	E1/21386.2933	950817	1226 / 3.359	12m	759m
E1/5511.2925	920804	E2/9228.2925	970127	1751 / 4.797	36m	253m
E1/8517.2933	930302	E1/21386.2933	950817	898 / 2.460	28m	325m
E1/21386.2933	950817	E2/9228.2925	970127	525 / 1.438	48m	190m
E1/25394.2925	960523	E2/5721.2925	960524	1 / tandem	109m	84m
E1/6284.2925	920927	E1/22660.2925	951114	1143 / 3.132	20m	456m
E1/24664.2925	960402	E2/4991.2925	960403	1 / tandem	111m	82m

Topography Removal

Topographic phase was removed by using either the 4-pass or the 2-pass/DEM method of topography removal depending on which method yielded the best results for each feature of interest. One-day tandem orbit pairs (the ERS-2 satellite orbit repeating the ERS-1 satellite orbit 24 hours later) were used in the 4-pass method to determine the topographic phase. The topographic phase was subtracted from the phase in each deformation pair by first scaling the unwrapped topographic phase by the ratio of the perpendicular components of the baselines between the deformation and topography pairs. Since the topographic phase must be unwrapped, high relief areas often cannot be completely unwrapped due to layover in which radar shadows exist on the leeward side of steep topography. These regions that cannot be unwrapped cannot be used to remove topography if the 4-pass method of topography is used. For the 2-pass method, 30-meter (1-arcsecond) resolution USGS DEMs were used to simulate the topographic phase and remove it from each deformation pair. In some cases the 4-pass topography removal did a better job of isolating the deformation signal of interest but in others, unwrapping errors masked signals of interest. For example, in track 127 frame 2925, the slip event on the San Andreas fault is well resolved, but unwrapping errors completely mask the slip signals on the Burnt Mountain and Eureka Peak faults and so the 2-pass/DEM method was used to image those signals.

RESULTS AND MODELS

Eureka Peak and Burnt Mountain Faults

Figure 3 shows the georeferenced interferogram (topography removed) from track 127, frame 2925 centered over the Coachella Valley. The two boxes identify the two regions of interest which are magnified in Figures 4 and 5 respectively. Figure 4a shows the northern region of interest magnified along with profile plots that transect both the Eureka Peak and Burnt Mountain faults at the three locations identified in the figure. It was found that the deformation pattern across the Eureka Peak and Burnt Mountain faults did not fit the expected right-lateral horizontal deformation pattern of range change stepping up from west to east across each fault[1]. What was found instead was a complex deformation pattern that included a dominant vertical signal between the faults. Since vertical deformation signals can mask horizontal signals due to the nearly 3-to-1 sensitivity difference between vertical and horizontal motion detection by the radar, the expected right-lateral range change pattern was not observed. Transect EPBM1, closest to the vertex of the two faults, indicates either uplift on the west side of the Burnt Mountain fault (BMF) relative to the east side, or subsidence on the east side relative to the west (modeling done of these two faults suggest the latter interpretation—see below). Transect EPBM2 shows the west side of the Burnt Mountain fault slightly down (or away) relative to the east side. This could be a transition to (expected) right-lateral motion which would show the west side range change lower (further away from the west-facing satellite look vector) than the east side. Most of the vertical offset here appears to have transferred over to the Eureka Peak fault as a relatively abrupt 1.5 cm drop to the east side of the fault. Transect EPBM3 shows the right-lateral signal increasing across the Burnt Mountain fault as the distance from the vertex between the two faults increases. The apparent lack of a corresponding reversal of phase color offset in the interferogram across the Burnt Mountain fault is due to an even color wrap (orange to orange) representing one complete fringe (28 mm vertical offset in range change) in the wedge region between the two faults. Fault parallel profiles done on either side of and between the two faults (not shown) support the fault crossing profile results and show an approximate 28 millimeter vertical (upward) step in the range change from north to south near the fault vertex.

The line-of-sight (los) range change displacement rate measured by the interferogram (~7.8 mm/yr) is significantly higher than the horizontal secular rate of 0.5-0.6 mm/yr determined from Holocene offsets [Jennings, 1994]. This is most likely due to most of the displacement occurring as continued after-slip after the Landers event since the date of the first orbit in the deformation pair is September 27th, 1992 (only three months after the Landers earthquake and within duration of high level aftershock activity). Hence the interferogram measurement does not represent the interseismic creep rate across the fault, but appears to have captured the after-slip displacement across the fault resulting from stress redistribution from the Landers rupture.

Southern Landers After-Slip Model

The Burnt Mountain and Eureka peak fault signals were modeled by including all coseismic Landers rupture zone fault segments and imposing a post-seismic slip distribution determined from GPS and creepmeter data [Hudnut, et al., 1994; Bodin, et al., 1994; Behr, et al., 1994]. Figure 4b shows the synthetic interferogram computed from after-slip distribution data sampled during the 3-year interval spanned by the interferogram (9/27/92-11/14/95). Caution must be used when interpreting the synthetic interferogram since abrupt color changes do not necessarily imply similarly abrupt phase changes. For example, the region

---

[1] Modeling reveals that simply imposing right-lateral slip on both faults produces the observed vertical deformation pattern seen in the interferogram, including the observed subsidence along the northern 1/3 of the wedge between the two faults.

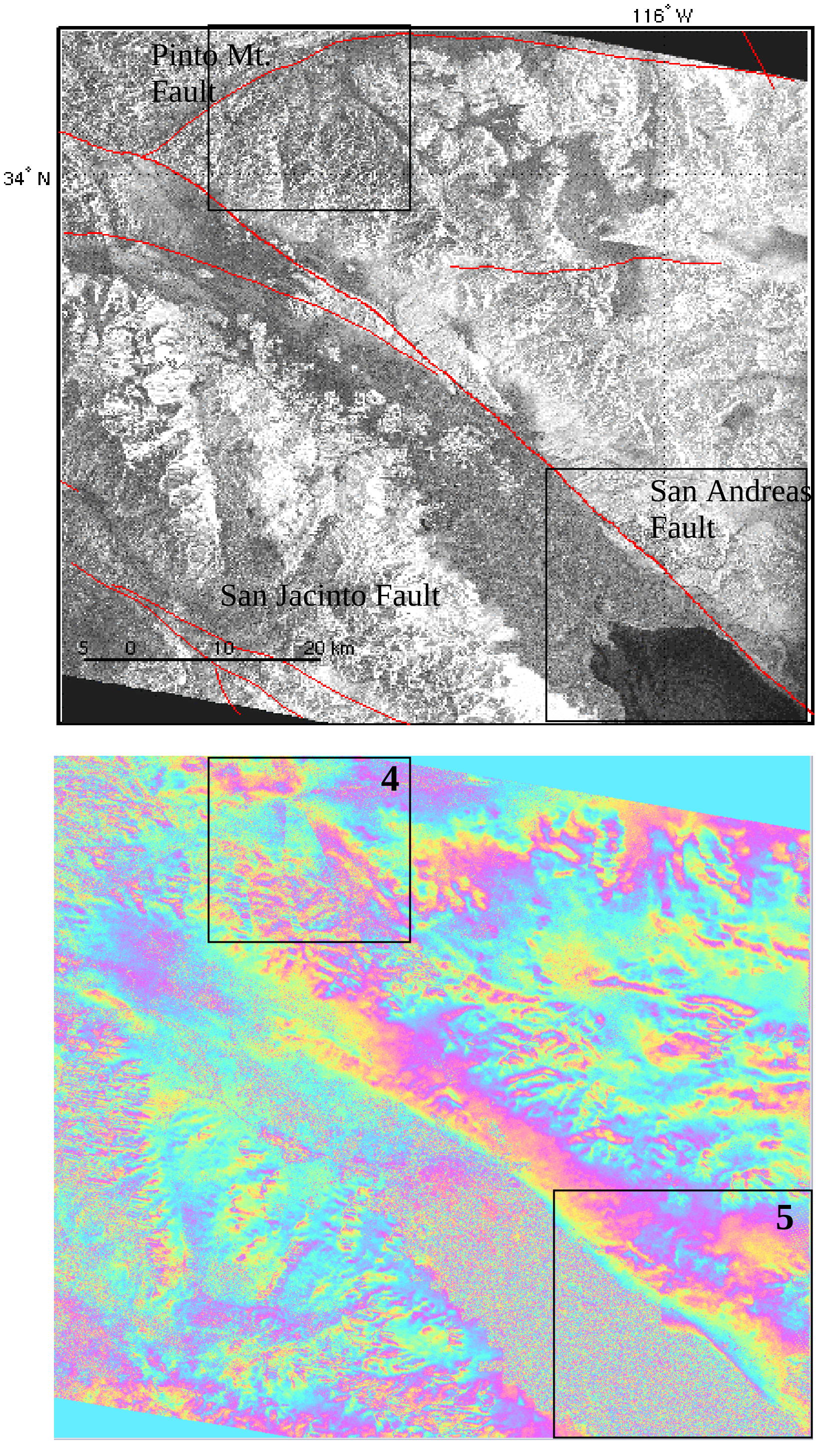

Track 127 Frame 2925

Figure 3: (top) Amplitude image of track 127, frame 2925 shown with the surface traces of the major faults in the region. (bottom) Deformation interferogram (topography removed) of orbit pair 22660_6284 for the same frame. Boxes denote regions of interest magnified in Figures identified by their respective figure numbers.

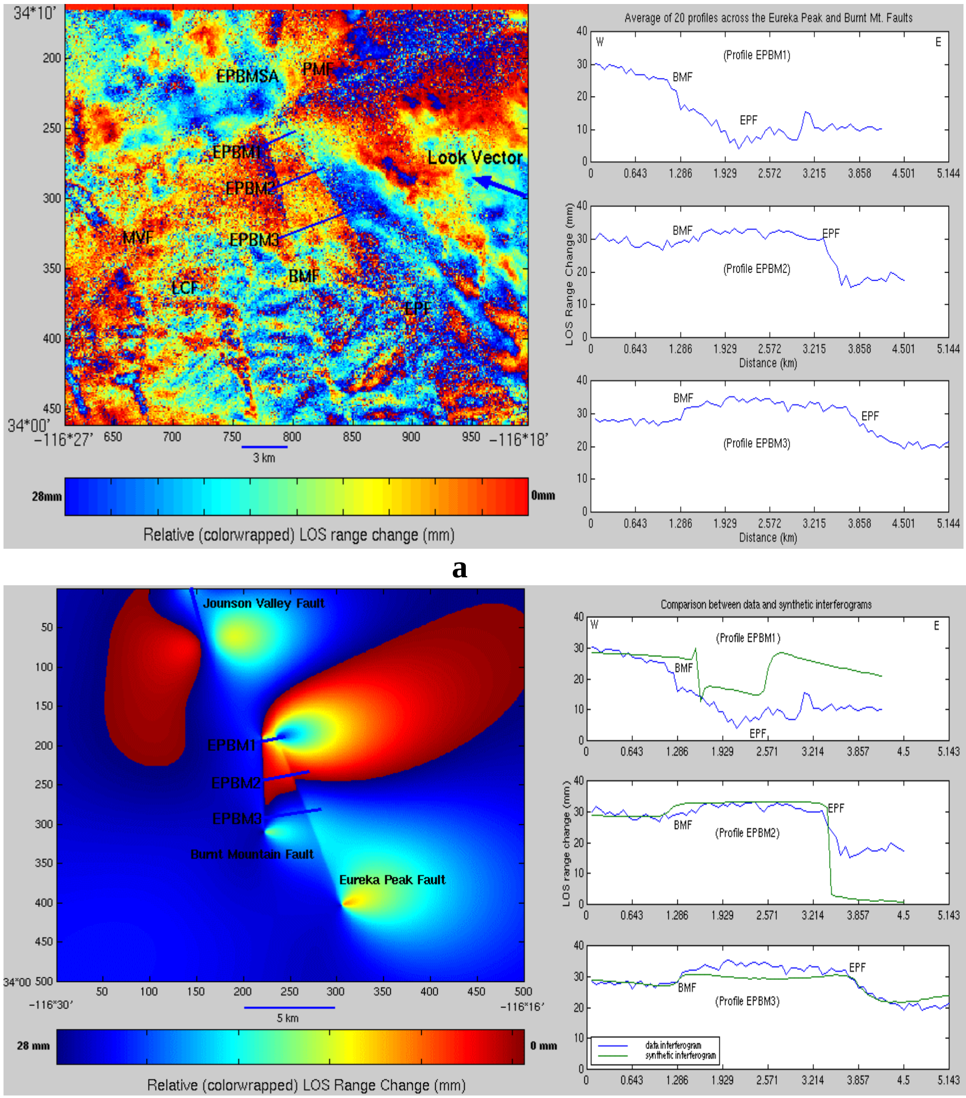

a

b

Best-fit model parameters
- 10cm dislocation from 0.05-10km depth on both BMF & EPF
- 15cm dislocation from 1-10km depth on southernmost 12km JVF

Figure 4: (a) Magnified view of northern area of interest in interferogram (box 4). Lines denote transects across the Eureka Peak and Burnt Mountain faults labeled according to: PMF=Pinto Mountain Fault; EPF=Eureka Peak Fault; BMF=Burnt Mt. Fault; JVF=Johnson Valley Fault; LCF=Long Canyon Fault; MVF=Morongo Valley Fault. (b) Synthetic interferogram of the Eureka Peak and Burnt Mountain faults shown with corresponding profile comparisons with data. One color cycle = 28 mm of range change.

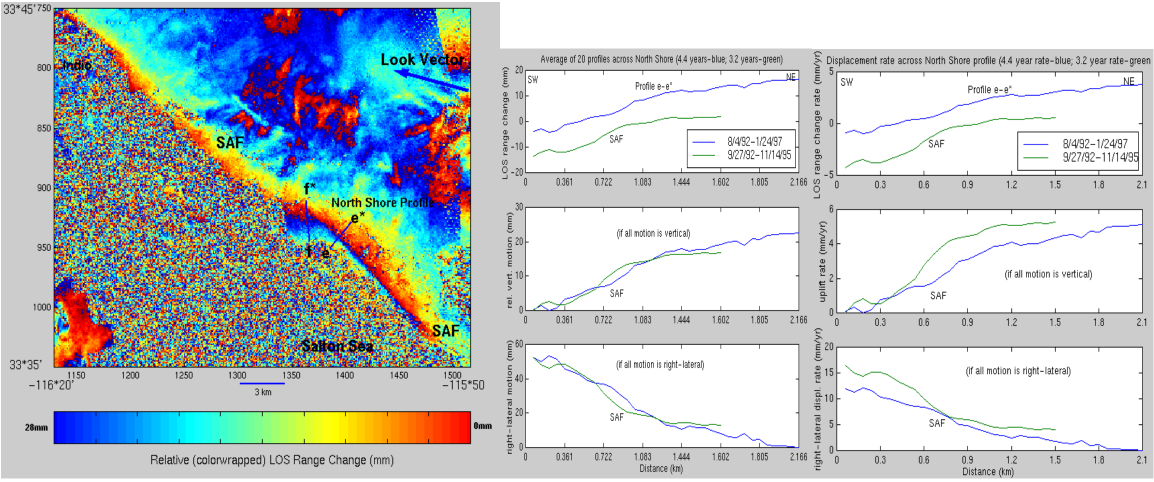

a

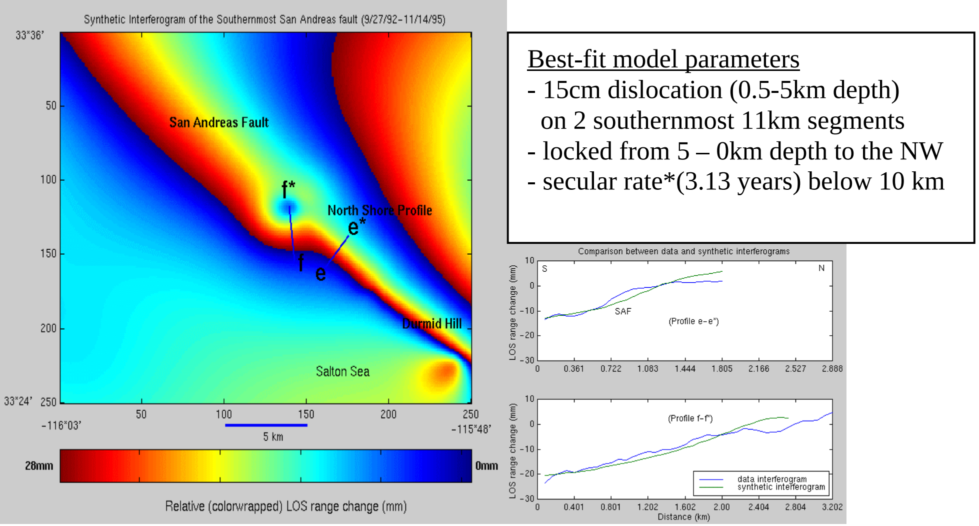

Best-fit model parameters
- 15cm dislocation (0.5-5km depth)
  on 2 southernmost 11km segments
- locked from 5 – 0km depth to the NW
- secular rate*(3.13 years) below 10 km

b

Figure 5. (a) Magnified view of southern area of interest in interferogram (box 5). Lines denote transects across the San Andreas Fault at strain tip (f-f*) and at North Shore (e-e*). (b) Synthetic interferogram of the San Andreas Fault slip along the southernmost Durmid Hill and North Shore segments shown with corresponding profile comparisons with data. One color cycle = 28 mm of range change.

between the faults from south-north changes abruptly from dark blue to red but it is a gradual change in range; the color wheel has simply wrapped back around to red. Figure 4b shows comparison plots between the model and data interferograms. The model predicts the gross shape and relative magnitude of the deformation across and between the faults with the exception of profile EPBM1 that crosses near the vertex of the two faults. In profile EPBM1 the anomalous low step between the two faults is predicted by the model and is a result of a complex stress distribution near the fault vertex, but it is more abrupt and narrower in extent in the model than it is in the data. Most of the region between the faults shows relative uplift resulting from two adjacent, converging right-lateral faults. This relative complex strain pattern is seen in both the data and synthetic interferograms.

Just northwest of the fault vertex a region of uplift is present in the model (dark blue and red circular region in the synthetic interferogram) that corresponds to the blue region of uplift seen in the data. In addition, the model also predicts the relative downward lobe corresponding to the relative down-warping yellow regions in the data. This yellow subsidence region is a result of the influence of the Johnson Valley fault terminating at this point which bifurcates the strain field into a bipolar form (i.e., upward motion on the west side indicated by blue and red, and downward movement on the east indicated by the yellow lobe). This was discovered by removing the Johnson Valley fault from the fault model which, when removed, also removed the yellow lobe and significantly altered the shape of the uplifted blue and red region.

The line-of-sight (los) range change displacement rate measured by the interferogram (~7.8 mm/yr) is an order of magnitude higher than the horizontal secular rate of 0.5-0.6 mm/yr determined from Holocene offsets [Jennings, 1994]. This is most likely due to most of the displacement occurring as continued after-slip from the Landers event since the date of the first orbit in the deformation pair (9/27/92) is three months after the Landers earthquake and within the period of relatively high aftershock activity. Thus, the interferogram measurements are not representative of the interseismic creep rate across the fault, but have captured the afterslip displacement across the fault resulting from stress redistribution from the Landers earthquake.

San Andreas Strain Anomaly (Track 127)

Figure 5a shows a magnified view of the southeast corner of the interferogram shown in Figure 3 where a very pronounced right-lateral creep signal can be seen along the San Andreas fault near the northeast shoreline of the Salton Sea. This signal is also seen in track 356, frames 2925 and 2933 to the south with similar absolute phase offsets measured in both frames (see profile plots in Figure 5a). This suggests that this anomaly may be due to one or more slip events rather than to accumulated interseismic strain. The location of this feature may suggest a transition point from right-lateral creep and transpression along the two southernmost Durmid Hill and North Shore segments of the San Andreas fault to the southeast [Bilham and Williams, 1985] to a locked condition along the Mecca Hills, Canal, and Indio segments to the northwest.

San Andreas Slip Event Model

A synthetic interferogram was constructed from models that attempt to reproduce both the anomalous strain lobe pattern seen at the northwest end of the signal and the observed range change across the San Andreas fault along the Durmid Hill and North Shore fault segments to the southeast. Figure 5b shows the synthetic interferogram formed from the best-fit model constrained by both the interferograms and by geodetic near-field and far-field data [need reference here]. The best fit model was a 15 cm slip dislocation from 0.5 km to 5 km depth along the southernmost two 11 km long Durmid Hill and North Shore segments of the San Andreas fault, while locking the upper 10 kilometers of the fault to the northwest. The 15 cm slip is interpreted be a triggered slip event following the June, 29th, 1992 Landers earthquake. since two overlapping interferograms measure the same absolute displacement even thought the length of time covered differs by1.2 years. Figure 5b shows a comparison plot of profiles e-e* and f-f*, the North Shore and strain tip profiles respectively, between the data and synthetic interferograms.

San Andreas Fault Strain Anomaly (Track 356)

Figure 6 shows the amplitude image and Figure 7 shows the time series of interferograms formed (topography removed) from track 356, frame 2925 centered over the

Salton Sea. A nearly identical strain tip signal is seen along the San Andreas fault near the north shoreline of the Salton Sea (see Figures 7b and 7d) as in Track 127 suggesting a single slip event occurred rather than continuous creep.

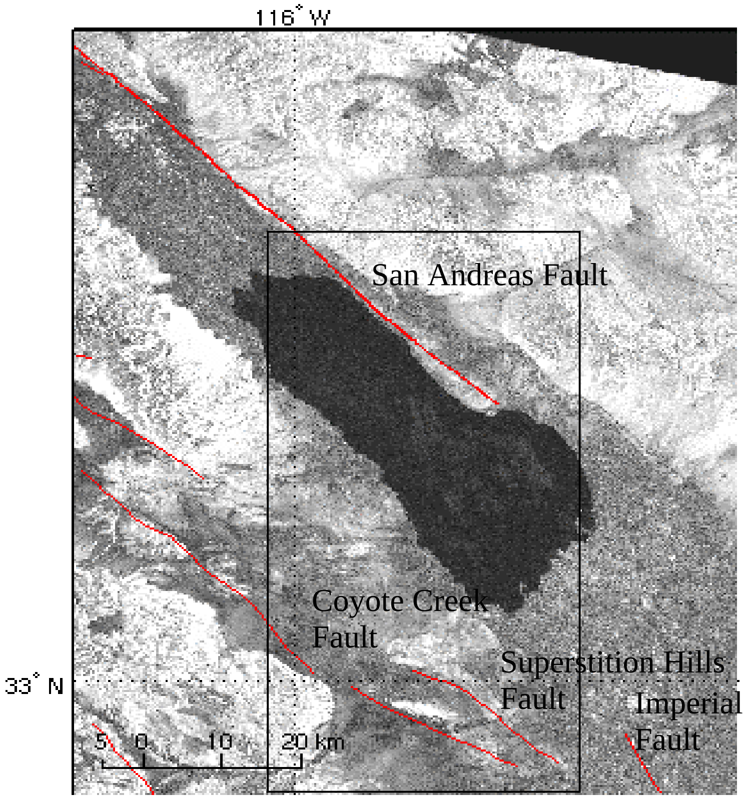

Track 356 Frame 2925

Figure 6: Amplitude image of track 356, frame 2925 shown with the surface traces of the major faults in the region. Boxed region denotes time series of deformation interferograms shown in Figure 7.

Superstition Hills Fault

Figure 7 shows a time series of four interferograms spanning the ’92 -’93, ’93 -’95, ’95 -’97, and ’92 – ‘97 epochs for the slip events on the San Andreas and Superstition Hills Faults. No slip was observed on either the San Andreas or Superstition Hills Faults in the ’92 – ’93 interferogram. Only minor slip is observed in the ’95 – ’97 interferogram. Most of the slip occurred on both faults in the ’93 – ’95 interferogram (4.31 ± 1.18 cm—well above the noise level). The ’92 – ’97 interferogram shows 4.07 ± 1.03 cm of slip on the Superstition Hills Fault, which agrees with the ’93 – ’95 pair to within the error estimate, suggesting the slip occurred during the ’93 – ’95 epoch. Unfortunately no ERS data is available for 1994 to further pinpoint the timing of the slip events. However, if the slip is averaged over the two years spanned by the ’93 – ’95 pair, an average slip rate of 2 cm/yr would still be an anomalous, transient rate of slip on an otherwise locked segment.

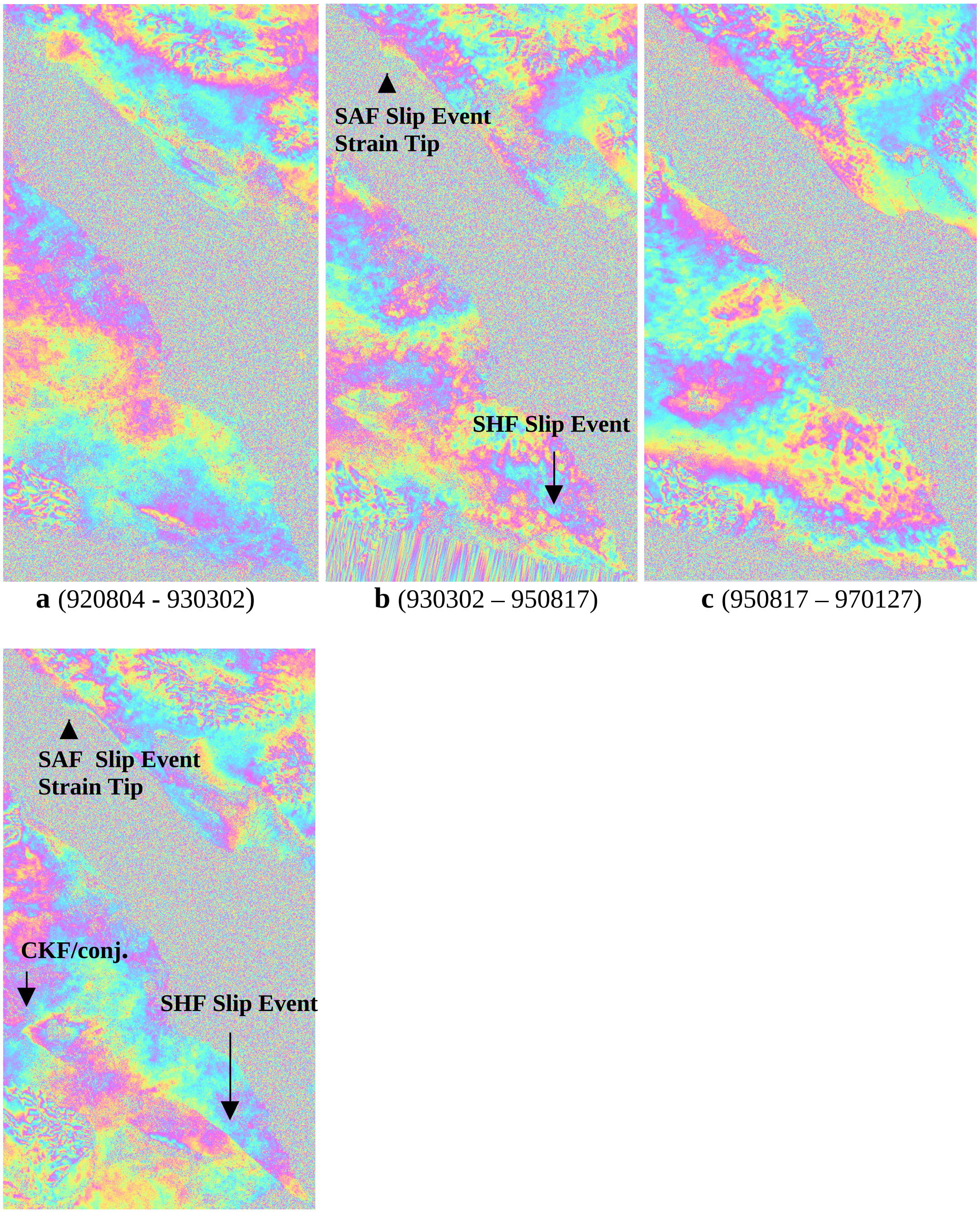

a (920804 - 930302) **b** (930302 – 950817) **c** (950817 – 970127)

d (920804 – 970127)

Figure 7: Time series of deformation interferograms of the boxed region shown in Figure 6. San Andreas Fault (SAF), Superstition Hills Fault (SHF) and Coyote Creek Fault (CKF)/conjugate fault slip events identified in figure.

SLIP AND SEISMIC MOMENT ANALYSIS

Figure 8 shows an overlay plot of right-lateral slip variation along strike of (parallel to) the Superstition Hills Fault for the three time series epochs and the ’92 – ’97 epoch. The ’93 – ’95 and ’92 – ’97 plots are very similar in both shape and magnitude, and are the only along-strike profiles that are well above the noise level, providing further evidence that the slip is constrained to the ’93 – ’95 epoch.

Table 2 shows equivalent seismic moments and earthquake magnitudes from the observed slip values on the Superstition Hills Fault for each epoch. Corresponding seismic moments from historical seismicity were also calculated for the same time intervals by summing the moments of all earthquakes in the vicinity of the fault assuming they all had right-lateral focal mechanisms and were located on the fault plane. This approximation overestimates the actual total moment released from recorded seismicity during these time intervals because most of the seismicity is not located on the fault planes. This procedure was done for both the southernmost segment of the San Andreas and the Superstition Hills Faults to provide a conservative comparison between the expected seismic moments from the slip events versus those from recorded seismicity. As can be seen in Table 1 the results for the Superstition Hills Fault shows that even by using this conservative comparison there is still at least 3 orders of magnitude difference between the expected seismic moments from the slip events versus those from recorded seismicity.

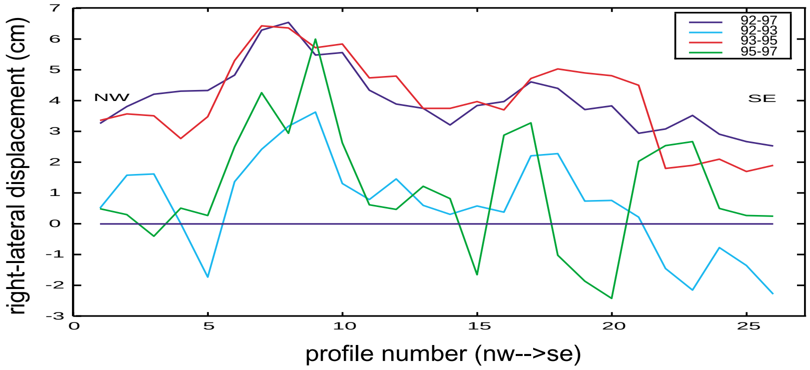

Figure 8: Overlay plot showing fault-parallel variation of right-lateral offsets across Superstition Hills Fault for each epoch.

Table 2 Comparison between slip, geodetically-determined seismic moment (Mo_g) and moment from summing historical seismicity (Mo_s), and corresponding equivalent earthquake magnitudes for the Superstition Hills Fault for each epoch

Epoch	ΔT (yrs)	Average Slip (cm)	Mo_g/Mo_s ($x10^{24}$ dyne-cm)	Mw_g/Mw_s
920804 - 970124	4.8	4.07 ± 1.03	1.22 / 0.00100	5.3 / 3.27
920804 - 930302	0.9	0.62 ± 1.55	0.02 / 0.00050	4.1 / 3.07
930302 - 950817	2.5	4.31 ± 1.18	1.29 / 0.00035	5.3 / 2.96
950817 - 970124	1.4	1.16 ± 1.95	0.03 / 0.00017	4.3 / 2.75

DISCUSSION

The slip events, if they occurred over earthquake rupture time scales (seconds) should have produced magnitude 5.3 and 5.6 earthquakes on the Superstition Hills and San Andreas Faults respectively but they did not. This observation leads to one of two possibilities. First, these two slip events did occur over earthquake time scales and for some anomalous reason, possibly due to the relatively thin (~5 km) seismogenic zone in the upper crust in the high heat flow Salton Trough region, seismic waves were not generated. Second, the slip events occurred over a longer time period within the 2.5 – year '93 – '95 epoch and represent an anomalous transient slip on otherwise locked fault segments that abruptly begins and ends during this time interval. This would be contrary to previous observations of aseismic moment release that occur mainly at interseismic strain rates (millimeters to centimeters per year for tens to hundreds of years) along creeping fault segments (e.g., Parkfield, CA). Either way, the implication for these findings are 1) that significant moment releases can occur over relatively short time periods without accompanying seismicity, and 2) that they may be missed by seismic and GPS networks and consequently not accounted for in seismic/strain budget calculations used in forecasting seismic hazards.

ACKNOWLEDGEMENTS

The author wishes to thank John Rundle and Roger Bilham who provided support through NASA and USGS grants respectively for this project, as well as funds to purchase ERS raw SAR data, while the author was a graduate student at the University of Colorado at Boulder. The author is also indebted to Howard Zebker (Stanford University) and Paul Rosen and others at the Jet Propulsion Laboratory, who developed the SAR processing software used in this study. Finally, the author is also indebted to Rick Ryerson (Institute for Geophysics and Planetary Physics (IGPP) at Lawrence Livermore National Laboratory) who provided support and funds to purchase additional SAR data to complete this work at LLNL.

This work was performed under the auspices of the U.S. Department of Energy by the University of California, Lawrence Livermore National Laboratory under Contract No. W-7405-Eng-48.

REFERENCES

Behr, J., R. Bilham, P. Bodin, and S. Gross, Eureka Peak fault after-slip following the 28 June 1992 Landers earthquake, *Bull. Seismol. Soc. Amer.*, vol. 84, pp. 826-834, 1994.

Bilham, R. and P> Williams, Sawtooth segmentation and deformation processes on the southern San Andreas fault, California, *Geophys. Res. Lett.*, vol. 12, no. 9, pp. 557-560, 1985.

Bodin, P.R., R. Bilham, J. Behn, J. Gomberg, K. Hudnut, Slip triggered on the southern California faults by the 1992 Joshua Tree Landers, and Big Bear earthquakes, *Bu;;. Seismol. Soc. Amer.*, vol. 84, pp. 806-816, 1994.

Burgmann R., E. Fielding, J. Sukhatme, Slip along the Hayward fault, California, estimated from space-based SAR interferometry, *Geology* 26, 559-62, 1998.

Goldstein, R.M., H. Engelhardt, B. Kamb and R. M. Frolich, Satellite radar interferometry for monitoring ice sheet motion: application to an Antarctic ice stream, *Science*, 262, 1525-1530, 1993.

Hanks, T.C., and C.R. Allen, The Elmore Ranch and Superstition Hills earthquakes of 24 November 1987: Introduction to the special issue, *Bull. Seismol. Soc. Am.*, vol. 79, pp. 231-238, 1989.

Hudnut, K.W., and M.M. Clark, New slip along parts of the 1968 Coyote Creek fault rupture, California, *Bull. Seismol. Soc. Am.*, vol. 79, pp. 451-465, 1989.

Hudnut, K.W., L. Seeber, and T. Rockwell, Slip on the Elmore Ranch fault during the past 330 years and its relation to slip on the Superstition Hills fault, *Bull. Seismol. Soc. Am.*, vol. 79, pp. 330-341, 1989.

Hudnut, K.W., and K.E. Sieh, Behavior of the Superstition Hills fault during the past 330 years, *Bull. Seismol. Soc. Am.*, vol. 79, pp. 304-329. 1989.

Hudnut, K.W., et. al., Co-seismic displacements of the 1992 Landers earthquake sequence, *Bull. Seismol. Soc. Amer.*, vol. 84, no. 3, pp. 625-645, 1994.

Larsen, S., and R. Reilinger, Global positioning system measurements of strain accumulation across the Imperial Valley, California: 1986 – 1989, *J. Geophys. Res.*, vol. 97, no. B6, pp. 8865-8876, 1992.

Louie, J.N., C.R. Allen, D.C. Johnson, P.C. Haase, S.N. Cohn, Fault slip on southern California, *Bull Seismol. Soc. Am.*, vol. 75, no. 3, pp. 811-833, 1985

Massonnett, D., et al., The displacement field of the Landers earthquake mapped by radar interferometry, *Nature*, vol. 364, 1993

Okada, Y., Surface deformation due to shear and tensile faults in a half-space, *Bull. Siesmol. Soc. Amer.*, vol. 75, mo. 4, pp. 1135-1154, 1995.

Peltzer, G., P. A. Rosen, Surface displacements of the 17 May 1993 Eureka Valley, California earthquake observed by SAR interferometry, *Science* 268, pp.1333-36, 1995

Prescott, W.H., M. Lisowski, J. Savage, Velocity field along the San Andrea fault in southern California, *Eos Trans., AGU*, vol. 68, no. 44 pp. 1506, 1987

Reilinger, R., A strain anomaly near the southern end of the San Andreas fault, Imperial Valley, California, *Geophys. Res. Let.*, vol. 12, no. 9, pp. 561-564, 1985..

Rosen, P.A., C. Werner, E, Fielding, S. Hensley, S. Buckley, P. Vincent, Aseismic creep along the San Andreas fault northwest of Parkfield, CA, measures by radar interferometry, *Geophys. Res. Lett.*, vol. 25, pp. 825-828, 1998.

Sieh, K.E., and P.L. Williams, Behavior of the southernmost San Andrea fault during the past 300 years, *J. Geophys. Res.*, vol. 95, no.B5, pp. 6629-6645, 1990.

Sharp, R.V., K.E. Budding, J. Boatwright, M.J. Ader, M.G. Bonilla, M.M. Clark, T.E. Fumal, K.K. Harms, J.J. Lienkaemper, D.M. Morton, B.J. O”Neill, C.L. Ostergren, D.J. Ponti, M.J. Rymer, J.L. Saxton, and J.D. Sims, Surface faulting along the Superstition Hills fault zone and nearby faults associated with the earthquakes of 24 November 1987, *Bull. Seismol. Soc. Am.*, vol.79, pp. 252-281, 1989.

Sylvester, A.G., R. Bilham, M. Jackson, S. Barrientos, Aseismic growth of Durmid Hill, southeasternmost San Andreas fault, California, *J. Geophyd. Res.*, vol. 98, pp. 14,233-14.243, 1993.

Vincent, P., J.B. Rundle, R. Bilham, S.M. Buckley, Aseismic creep along the San Andreas and Superstition Hills, faults, with uplift at Durmid Hill, southernmost San Andreas fault, CA, measured by radar interferometry, SCEC, 1998 annual meeting, p. 92.

Vincent, P., J.B. Rundle, R. Bilham, S.M. Buckley, Aseismic creep along the San Andreas and Superstition Hills faults with uplift at Durmid Hill, southernmost San Andreas fault, CA measured by radar interferometry, EOS trans., AGU, 79, 45, 1998.

Vincent, P. Application of SAR Interferometry to Low-Rate Crustal Deformation Fields, Ph.D. Thesis, University of Colorado, 1998.

Wesnousky, S.G., Earthquakes quaternary faults, and seismic hazards in southern California, *J. Geophys. Res.*, vol. 19, pp. 12,587, 12,631, 1986.

Zebker, H.A., P.A. Rosen, R.M. Goldstein, A. Gabriel, and C.L. Werner, On the derivation of coseismic displacement fields using differential radar interferometry: The Landers earthquake, *J. Geophys. Res.*, vol. 99, pp. 19,617-19,634, 1994.